Journal of Applied Fluid Mechanics, Vol. 18, No. 5, pp. 1189-1204, 2025.
Available online at www.jafmonline.net, ISSN 1735-3572, EISSN 1735-3645.
https://doi.org/10.47176/jafm.18.5.3093

Numerical Analysis of the Inlet and Outlet Diameter Effects on Pulsation Dynamics and Cavitation in the Lobe Pump

H. Zhou[1], P. Zhou[1, 2†], L. Meng[2], J. Li[1], C. Xiang[3] and H. Qian[3]

[1] *College of Metrology Measurement and Instrument, China Jiliang University, Hangzhou, 310018, China*
[2] *Key Laboratory of River Basin Digital Twinning of Ministry of Water Resources, Beijing, 310018, China*
[3] *School of Mechanical Engineering, Zhejiang University of Water Resources and Electric Power, Hangzhou 310018, China*

†*Corresponding Author Email: zhoupj@cjlu.edu.cn*

ABSTRACT

To investigate the impact of inlet and outlet diameters on the performance of lobe pumps, this paper analyses six lobe pumps with an inlet and outlet diameter ratio of 1, as well as five lobe pumps with varying inlet and outlet diameter ratios, while keeping other conditions constant. Three-dimensional unsteady numerical simulations of the pumps were conducted using the full cavitation model and the re-normalization group (RNG) *k-ε* turbulence model. The results show that for the lobe pumps with internal diameters between 40 mm and 100 mm, the shaft power is reduced by 17.6%, the pressure is reduced by 0.4 MPa, the pulsation coefficient is reduced by 18%, the variation of the gas volume fraction at the gap is in the range of 0.2 to 0.8, and the maximum value of the radial force in the X-direction decreases from 58.36 to 17.6 kN, and that the maximum value of the radial force in the Y-direction decreases from 14.56 to 3.25 kN. When the scale is increased from 0.6 to 1, the shaft power decreases by 25.9%, the pressure decreases by 0.1 MPa, the pulsation coefficient decreases by 6%, the volume fraction of gas at the gap varies between 0.1 and 0.8, and the maximum radial force in the X-direction decreases from 17.63 to 12.52 kN, and in the Y-direction decreases from 7.68 to 6.32 kN. This shows that choosing a suitable inner diameter can reduce the cavitation tendency of the lobe pump, enhance its anti-cavitation ability, optimize the fluid flow characteristics, and thus improve its reliability and stability.

Article History

Received August 30, 2024
Revised November 4, 2024
Accepted December 14, 2024
Available online March 4, 2025

Keywords:

Lobe pumps
Inlet diameter
Outlet diameter
Cavitation
Shaft power
Pressure pulsation
Dynamic grid technique

1. INTRODUCTION

Lobe pumps are integral components in hydraulic systems, where their performance characteristics critically influence the overall system's efficiency and reliability (Li et al., 2024b). In recent years, with the improvement of environmental protection and energy efficiency requirements, lobe pump performance has received increasing attention (Li et al., 2019; Gu et al., 2021; Zhai et al., 2022). Among the key design parameters, the hydraulic diameter ratio plays a pivotal role in determining pump efficiency. The accurate performance prediction of lobe pumps is essential for researchers and developers, enabling them to assess design efficacy, reduce development time, and lower costs. Currently, three primary methods are adopted for predicting pump performance. (1) Computational fluid dynamics (CFD) software (Dehghan et al., 2024), such as PumpLinx, Fluent, CFX, and STAR-CCM+ (Dehghan & Shojaeefard, 2022; Zhou et al., 2025), is used to simulate and predict pump performance (Wang et al., 2018; Qiu et al., 2022; Orlandi et al., 2023). (2) Machine learning methods, particularly neural networks, are employed for performance prediction (Vande Voorde et al., 2004; Luo et al., 2025; Li et al., 2024a). (3) Theoretical and empirical formulas are applied to calculate performance losses (Sun et al., 2022).

The most commonly utilized approach today is the first method, which involves three-dimensional modelling to create a fluid domain, generate a high-quality mesh, and set simulation parameters. This method demands precision in aspects such as the model dimensions, parameter configurations, and mesh quality. Its advantages include the ability to visually assess variable changes – such as pressure and velocity – through cloud diagrams and vector plots, making comparisons easier and the outcomes more convincing (Bonandrini et al., 2012; Matteo et al., 2019). The second method, while efficient, suffers from lower result accuracy and experimental feasibility, as it requires

NOMENCLATURE

$2a$	centre distance	R_c	rates of vapor routing
CAB	conformal adaptative binary-tree	R_e	rates of vapor generation
C	empirical constant	R_g	roll radius
C_c	routing coefficients	R_m	radius of the leaf top circle
C_e	vapor generation	T	time
D_f	vapor diffusion coefficient.	$\vec{u}$	velocity vector of the fluid
f	vapor mass fraction	$\vec{u}_s$	deformation velocity for dynamic mesh
Fx	radial force in x direction	Y_M	total dissipation rate
Fy	radial force in y-direction	Z	blade number
Fz	axial force in z direction	δV	boundary of the control volume
G_b	buoyancy turbulent energy	δ	rotor gap
G_k	velocity turbulent kinetic energy	ε	dissipation rate
k	turbulent kinetic energy	μ_{eff}	correction factor
L	rotor axial length	ρ	fluid density
N	rotor speed	Γ	diffusion coefficient
P	pressure	ω	helix angle
Q	flow rate	Ω	control volume
R_0	radius of the roll circle	$\overline{S_{ij}}$	strain rate tensor

extensive datasets for training and relies on deep learning through multi-layer neural networks. The third uses empirical and theoretical formulas to calculate depletions, summarizing empirical data to estimate internal fluid losses. However, the limitations of this approach are evident due to its reliance on generalized formulas.

Current research on vane rotor pumps has focused on rotor profiles and media viscosity, with fewer considerations made to real operating conditions and rotor connecting components, notably inlet and outlet designs. The hydraulic diameter ratio (defined as the ratio of the inlet and outlet diameters of the pump) plays a key role in the performance of vane pumps in terms of flow rate, head, efficiency, and noise level. However, investigations on how the inlet and outlet diameters affect the performance of vane pumps are still limited, and most researchers' setups in this regard are either empirical or derived from pump similarity theory (Al-Obaidi, 2024a).

In this paper, a transient numerical simulation of a vane rotor pump was carried out using a dynamic mesh technique to predict the effect of inlet and outlet diameters on the shaft power, excitation force, and pressure pulsation of a vane rotor pump with all other conditions held constant (Li et al., 2023, Li et al. 2024c). The influence of altering the inlet and outlet diameters on cavitation, pulsation, and shaft power as well as radial and axial forces was investigated (Al-Obaidi, 2024b; Al-Obaidi & Alhamid, 2024; Al-Obaidi et al., 2024). The results showed that the pulsation, axial power, and excitation force were affected to varied degrees by the change in inlet and outlet diameters when the ratio of the inlet and outlet diameters was one. For input and exit diameters between 40 mm and 100 mm, the pressure reduced by 0.4 MPa, the pressure pulse coefficient decreased by 18%, and the axial power decreased by 16.6%. In the range of intake and exit diameter ratios from 0.4 to 1, the pressure reduced by 0.1 MPa, the pressure pulse ratio decreased by 6%, and the shaft power decreased by 25.9%. This study provides reference and technical assistance for cavitation suppression and performance enhancement in fluid mechanics with the purpose of attaining better suppression in engineering applications.

2. GEOMETRIC AND NUMERICAL SIMULATION MODELS

2.1 Geometric Models

This paper focuses on the lobe rotor pump, a type of rotary displacement pump. Gear-driven rotor motions alter the pump cavity's internal volume, thereby creating varying chamber pressures and vacuums. This variation enables the pump to harness energy efficiently. The pump comprises several primary components: the lobe rotor, the pump body, and the front and rear end covers, as well as the active and driven shafts, couplings, and seals, among others (Zhai et al., 2022).

The rotor profile of the rotary lobe rotor pump is used as a pendulum rotor profile, and the actual profile equation of the reference pendulum rotor is (Liu et al., 2012; Jacazio & De Martin, 2016; Zhou et al., 2023):

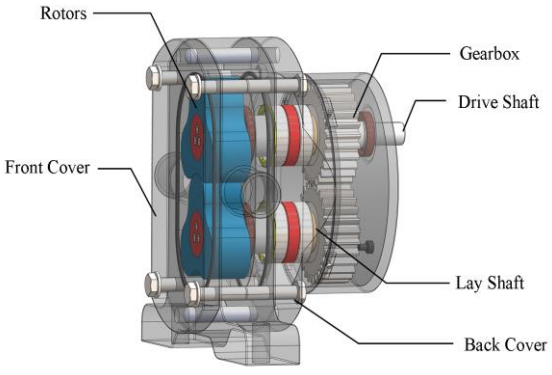

Fig. 1 Schematic diagram of lobe pump structure

Table 1 Structure parameters and work condition of pump

Name of the parameters	Value
Radius of leaf top circle	100 mm
Center distance	150 mm
Roll radius	12.5 mm
Rotor gap	0.1 mm
Inlet pressure	0.1 MPa
Outlet pressure	0.5 MPa
Rated Speed	400 r/min
Axial length of rotor	102 mm
Blade number	3

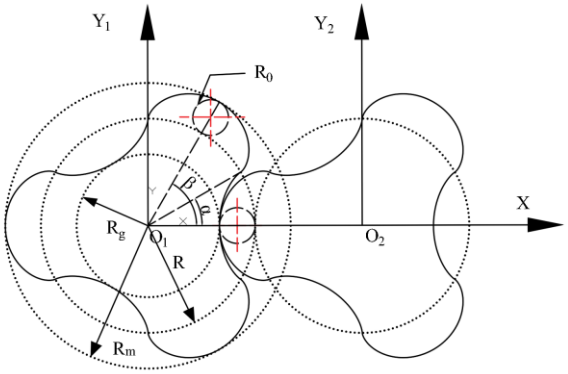

Fig. 2 Schematic diagram of three-lobe pendulum line

$$\begin{cases} x=\dfrac{(2z+1)R_m}{2(z+1)}\cos\theta+\dfrac{R_m}{2(z+1)}\cos[(1+2z)\theta]+\dfrac{\delta}{2}\cos[(z+1)\theta] \\ y=\dfrac{(2z+1)R_m}{2(z+1)}\sin\theta+\dfrac{R_m}{2(z+1)}\sin[(1+2z)\theta]+\dfrac{\delta}{2}\sin[(z+1)\theta] \end{cases} \tag{1}$$

$$\begin{cases} x=\dfrac{(2z\text{-}1)R_m}{2(z+1)}\cos\theta\text{-}\dfrac{R_m}{2(z+1)}\cos\left[(1\text{-}2z)\theta\right]\text{-}\dfrac{\delta}{2}\cos\left[(z\text{-}1)\theta\right] \\ y=\dfrac{(2z\text{-}1)R_m}{2(z+1)}\sin\theta\text{-}\dfrac{R_m}{2(z+1)}\sin\left[(1\text{-}2z)\theta\right]+\dfrac{\delta}{2}\sin\left[(z\text{-}1)\theta\right] \end{cases} \tag{2}$$

Based on the relationship between the parameters, the equations for this type of line were designed as shown in Table 1:

Based on the literature, it is determined that the value of α ranges from 0.7 to 1.3, and α is the ratio of the radius of the leaf top circle to the axial length of the rotor (Li et al., 2018). In this paper, an α of 0.98 is used. In Fig. 2, R_m is the radius of the leaf top circle, R_0 is the radius of the roll circle, R_g is the radius of the roll, and O_1O_2 is the centre distance. In Fig. 3, the inlet and outlet positions as well as the rotor axial length (L) are labelled.

2.2 Computational Model

2.2.1 Turbulence Model

In this paper, the changing law of the internal flow field of a three-lobe cycloidal rotor pump is investigated

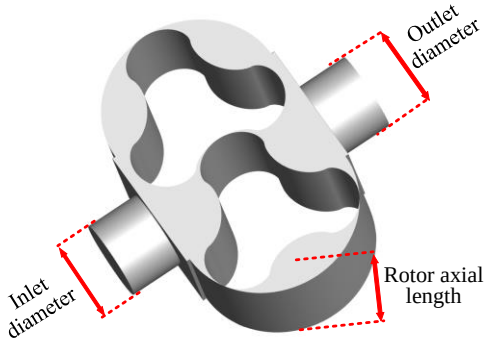

Fig. 3 Fluid domain model of the lobe pump

by using PumpLinx simulation software and setting up a transient simulation. Since the operating principle of the rotor pump makes its internal flow change dynamically over time, transient simulation can precisely capture the details of this process to ensure that the dynamic behaviour of the fluid is accurately reflected. Therefore, the choice of transient simulation is aimed at better understanding the evolution of the flow field over time. As PumpLinx is a software designed for rotating machinery and fluid systems, its automatic mesh generation function can be based on the pump's geometric characteristics and operating environment to quickly generate high-quality mesh, thus improving the simulation accuracy and shortening the simulation time required.

The flow field inside the loobe pump is extremely complex, with an output Y+ value of 128.24, which requires the introduction of a turbulence model to solve. The two commonly used solution methods are the standard k-ε turbulence and the re-normalization group (RNG) k-ε turbulence models, both of which involve the Reynolds-averaged Navier–Stokes (RANS) equation model. The basic principle of the RANS model is to decompose the instantaneous physical quantities into averaged and pulsating components for calculation. The Reynolds-averaged Navier-Stokes equations are derived by time-averaging the velocities and pressures (Li et al., 2018).

$$\rho\frac{dk}{dt}=\frac{\partial}{\partial x_j}\left(\alpha_k\mu_{eff}\frac{\partial k}{\partial x_j}\right)+2\mu_i S_{ij}\frac{\partial\overline{u_i}}{\partial x_j}-\rho\varepsilon \tag{3}$$

$$\rho\frac{d\varepsilon}{dt}=\frac{\partial}{\partial x_j}(\alpha_\varepsilon\mu_{eff}\frac{\partial\varepsilon}{\partial x_j})+2C_{1\varepsilon}\frac{\varepsilon}{k}\nu\overline{S_{ij}}\frac{\partial\overline{u_i}}{\partial x_j}-R-C_{2\varepsilon}\rho\frac{\varepsilon^2}{k} \tag{4}$$

where G_k is the turbulent kinetic energy production term, C is an empirical constant, $\overline{S_{ij}}$ is the strain rate tensor; α_k, α_ε are the Prandtl numbers corresponding to the turbulent kinetic energy k and dissipation rate ε; ρ is the density; and μ_{eff} is the correction factor.

2.3 Cavitation Models

The cavitation models include the constant gas mass fraction, equilibrium gas dissolution, variable gas mass fraction, gas dissolution, and full cavitation types (Zhao et al., 2023; Chen et al., 2024a).

$$\begin{cases} R_c = C_c \rho_l \rho_v \left[\dfrac{2}{3} \dfrac{(P - P_V)}{\rho_i} \right]^{\frac{1}{2}} f \\ \dfrac{\partial}{\partial t} \int \Omega(t) \rho f d\Omega + \int \sigma \rho \left((v - v_\sigma) n \right) = \\ \int \sigma \left(D_f + \dfrac{\mu_t}{\sigma_f} \right) (\nabla f n) d\sigma + \int \Omega (R_e - R_c) d\Omega \\ R_e = C_e \rho_l \rho_v \left[\dfrac{2}{3} \dfrac{(P - P_V)}{\rho_i} \right]^{\frac{1}{2}} (1 - f - g_f) \end{cases} \tag{5}$$

where ρ is the fluid density, Ω is the control volume, f is the vapor mass fraction, σ is the fluid surface tension, and D_f is the vapor diffusion coefficient. R_e and R_c are the rates of vapor generation and routing, and C_e and C_c are the vapor generation and routing coefficients, respectively.

In this paper, the volume fraction change in the dynamics of gas bubbles inside the liquid is studied. The gas mass fraction or the equilibrium gas dissolution models cannot be used to examine this problem. The full cavitation model considers not only the air in the liquid but also the vapor, which is more suitable for the cavitation process of the circular spiral lobe pump under high-speed and high-pressure working conditions. By comparing the theoretical model with the experimental results, the full cavitation model can better analyse the undissolved gas bubbles. Therefore, we selected the full cavitation model (Hatano et al., 2014; Chen et al., 2024b; Malekshah et al., 2024).

$$\begin{aligned} &\frac{\partial}{\partial t} \int \Omega(t) \rho f d + \int \sigma (\rho (v - v_\sigma) n) = \\ &\int \sigma \left(D_f + \frac{\mu_t}{\sigma_f} \right) (\nabla f n) d\sigma + \int \Omega (R_e - R_c) d\Omega \end{aligned} \tag{6}$$

2.4 Dynamic Grid

The rotor in the movement process of the rotor cavity along with the rotor of the relative rotational movement changes can be utilized to achieve the movement process of the sliding mesh technique. The essence of its movement is also that of the grid; however, the slip mesh can only be used to calculate the movement in the region with the problem analysed, as in the area within the boundaries where the movement follows different rules, the situation cannot be determined. Dynamic mesh is the true sense of moving mesh movement nearest to the real physical condition. Consequently, this study adopts a dynamic mesh model that adapts the fluid domain mesh according to the rotor's rotation (Menendez Blanco & Fernandez Oro, 2012; Liersch et al., 2014; Ammendolea et al., 2023; Meng et al., 2023). This model employs the two rotors as motion boundaries and treats the outer pump body as rigid, while designating the remaining components as walls. Furthermore, a user-defined driver manipulates the rotors' motion by specifying the rotation centre, direction, and speed.

The dynamic mesh algorithm facilitates an in-depth analysis of dynamic changes in flow, pressure, and velocity. It accurately calculates fluid movement, considering both the rigid motion of the fluid domain's boundary and the deformation of flexible boundaries over time. This approach, therefore, offers a more accurate reflection of flow field characteristics. For each boundary in the flow field, its motion obeys the following law (Liu et al., 2015):

$$\frac{d}{dt} \int_\gamma \rho \phi dV + \int_{\delta V} \rho \phi (\vec{u} - \vec{u}_s) d\vec{A} = \int_\gamma S_\phi dV + \int_{\delta V} \Gamma \nabla \phi d\vec{A} \tag{7}$$

Where $\vec{u}$ is the velocity vector of the fluid; $\vec{u}_s$ is the deformation velocity for dynamic mesh; S_ϕ is the flux source term; Γ is the diffusion coefficient; and δV is the boundary of the control volume.

2.5 Mesh Delineation and Independence Check

Prior to meshing, the fluid domain was divided into three regions: the inlet, outlet, and rotor. Based on PumpLinx's meshing methodology, the inlet and outlet sections of the fluid domain are mesh-generated using its unique conformal adaptative binary tree (CAB) algorithm. This can automatically adjust the mesh scale according to the geometric features. The generation speed is fast and the quality is high. In this paper, the maximum mesh scale is set to 0.002, the minimum is 0.0008, and the relative mesh scale of the surface is 0.001.

For the rotation region, a generic grid template in the software is used for meshing. Unlike traditional advective meshes, this template is based on Cartesian coordinates for cell delineation and numerical calculations by the finite volume method. For the selection of mesh size in the rotor region, a customized mode is utilized to adjust the gap and the overall mesh distribution by controlling the number of mesh layers in the axial, radial, and circumferential directions. In this study, the number of mesh layers in the circumferential direction is set to 360, with 16 layers in the radial one and 60 layers in the axial one.

After meshing, it is critical to verify the independence of the mesh as well as the time step to ensure optimal quality and prevent any adverse effects on the simulation results. As depicted in Fig. 4, the overall grid error is less than 5%, and the time step error is less than 1%. The simulation results show that the most stable outcomes are obtained when the number of grids is between 1.14 million and 1.88 million and the time step is at 0.0006. In this work, the grid number of 1.14 million and the time step of 0.0006 are chosen as the parameter settings for numerical simulation. The specific fluid domain grid model and grid independence verification are presented in Figs. 4 and 5.

Figure 5 A shows an enlarged view of the rotor gap. Figure 5 B shows the meshing of the rotor inlet and rotor intersection. The CAB algorithm avoids the large increase in the number of meshes and computational time normally associated with multi-layer meshing (Jacazio & De Martin, 2016; Xu et al., 2024). This approach also minimizes the risk of negative volumetric mesh errors. However, using too few mesh layers can hinder subsequent analyses and image processing, which may lead to undesirable results.

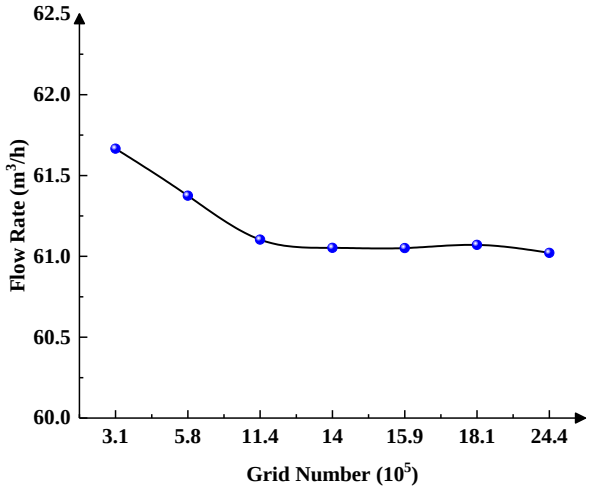

(a) The independence of the grids

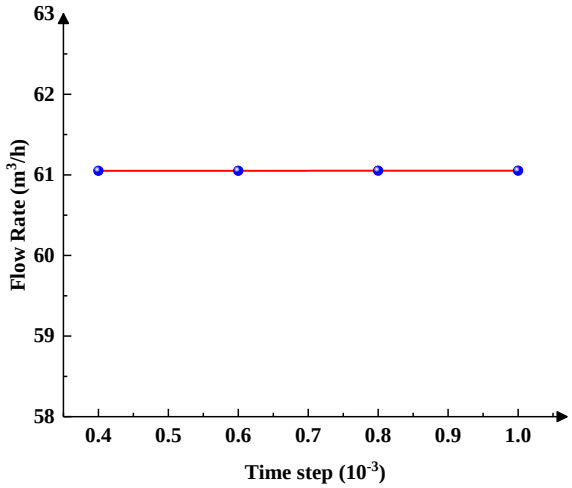

(b) The independence of the grids

Fig. 4 Grid and time step independent verification

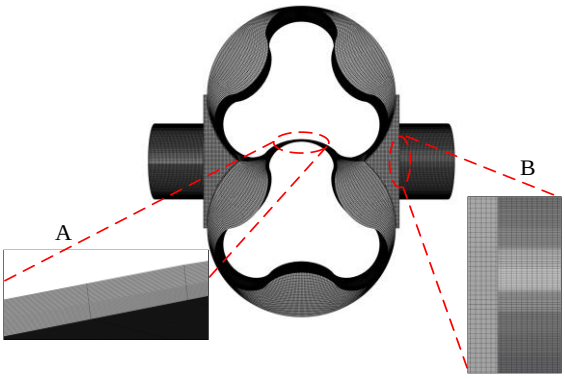

Fig. 5 Mesh model of the pump

3. NUMERICAL CALCULATION

3.1 Boundary Conditions

In this study, we use preset pressure boundary conditions at the inlet and outlet. The inlet and outlet pressures are kept constant to match the rated conditions. The rotor wall is designated as a rotating wall, while all other walls are set as stationary ones, and the interfaces between the components are connected by mismatched grid interface (MGI) faces. The direction of the rotation of the rotor of the lobe pump is set, and the number of rotor revolutions is calculated to be four revolutions in total. After its operation is stabilized, the total cavitation model is then added to ensure that it is realistic and reliable. The conveying medium is clear water at room temperature, the reference pressure of the liquid is 101325 Pa, the dynamic viscosity is 0.001003 Pa/s, the volume fraction of the gas is 2.3e-05, the saturated vapor pressure is 3610 Pa, and the positive inlet pressure is 0.1 MPa.

In this paper, we adopt the transient simulation method for simulation. This involves the setting of the time step, which is the interval between the completion of each iteration in the calculation of the solution. A small time step can improve the simulation accuracy at the cost of more time; a large time step can be accompanied by errors in the negative volume mesh and instability of the simulation results. After analysing the entrance speed and the mesh accuracy of the model, the time step is usually one to two orders of magnitude smaller. In this work, the time step is set to be every 1°, i.e., 0.0006 (Sun et al., 2022). In order to investigate the effects of various design parameters on the performance of the rotor lobe pump, the pressure pulsation at the pump outlet, cavitation at the gap, and the force and torque of the rotor in the x, y, and z directions are monitored. The convergence determination of this software is set to 0.1; when the monitored pump outlet flow and force curves show periodic fluctuations, it is considered that the calculation has been converged, and the smoothed portion of the monitored convergence is used for correlation analysis.

3.2 Experimental Verification

In order to verify the correctness of the numerical simulation results, Fig. 6a shows the flow rate magnitude under different grid numbers in the literature with my simulation results of Fig. 4a with an error of less than 5%. Figure 6b shows the axial force applied to the straight rotor and helical rotor, and it is seen that the axial force z-axis direction of the straight rotor is 0, and the simulation test result in this paper is also 0 in the z-axis direction. The simulation results were compared with those from the literature and showed high consistency, confirming the accuracy of the numerical simulation method used in this study. In addition, the literature investigated the flow rate of the lobe pump under various rotational speeds and outlet pressures using a closed-loop test rig. The experimental procedure involved controlling the outlet pressure by adjusting a ball valve at specific rotational speeds and measuring the outlet flow rate with a flow meter. Once the pressure was maintained at a constant level, the rotational speed was controlled by adjusting the frequency of the geared motor, and the flow rate was recorded with a flow meter (Zhang et al., 2019).

Figure 6c depicts the pressure variations as well as the performance test and numerical calculation results for a cycloidal rotor lobe pump with a rotor diameter-to-length ratio of 0.98. After adjusting the size of the export pressure value, the export pressure of the lobe pump and the export flow rate P-Q characteristic curve show a linear decreasing distribution, and the numerical prediction of the export flow rate is 2.3%-4.6% larger than the experimental measurement value. By adjusting the rotational speed, the

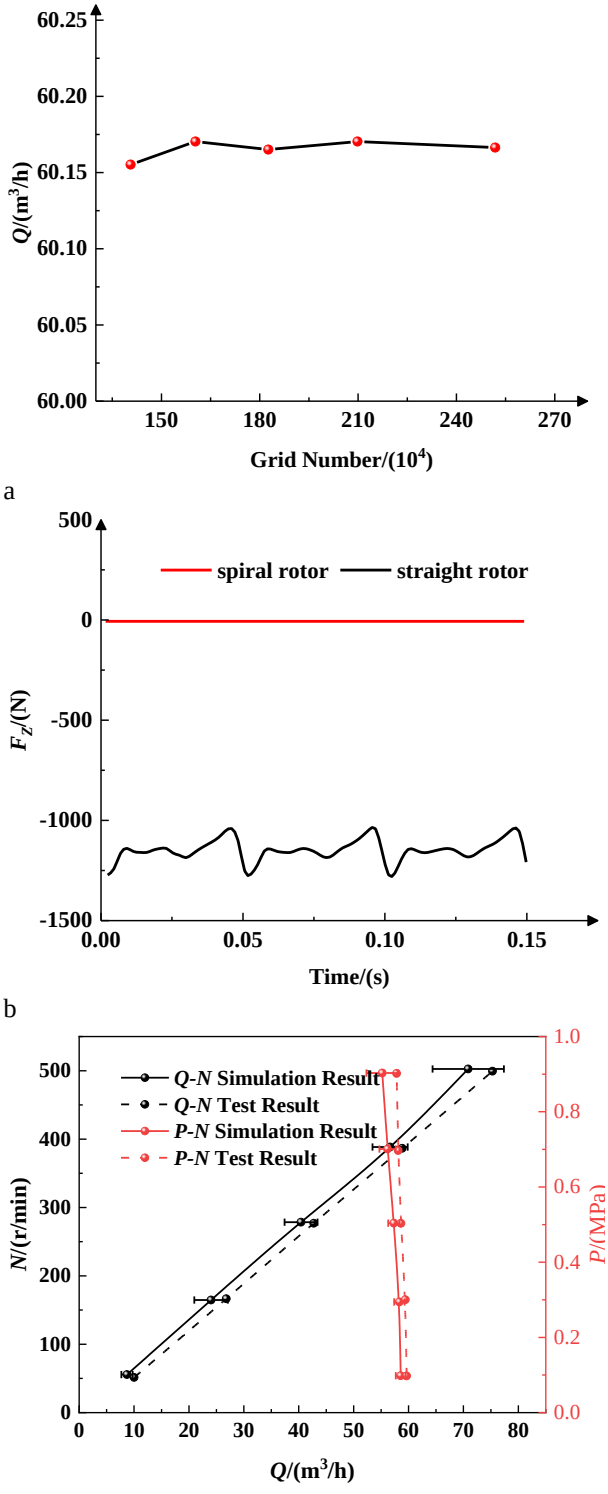

Fig. 6 Comparison of numerical simulation and experimental results

speed of the lobe pump and the export flow rate N-Q characteristic curve demonstrate a linear increasing distribution, with an error of 4%-5.2% between the numerical calculation result and the experimental one. The reason for the error is analysed, and it may be the loss of volume caused by the leakage of the rotor at the gap during rotation and the leakage at the end face. There is also the fact that the turbulence and cavitation models are only used to add to the model without taking into account the loss of mechanical energy and the generation and dissipation of heat energy when the rotor is rotating in the actual process. However, considering the overall outcomes, the error results are within a reasonable range. Therefore, after investigating whether the lobe pump performance design indicators meet the design needs and whether the numerical prediction results have a high degree of accuracy, these outcomes prove that the model can be applied and that the numerical prediction methods can be employed.

Table 2 Ratio 1 hydrodynamic diameter parameter configuration

Cases	Inlet diameter (mm)	Outlet diameter (mm)	Diameter ratio
1	40	40	1
2	60	60	1
3	70	70	1
4	85	85	1
5	90	90	1
6	100	100	1

3.3 Numerical Simulation Scheme Design

The turbulence model used is the RNG *k-ε* one, which is modified for the standard *k-ε* version in the CFD software. It takes into account the rotational and cyclonic flow in the mean flow and provides an analytical equation considering the viscosity of the low Reynolds number flow, which can effectively deal with the high strain rate and the flow line curvature of the larger movement. The hydraulic diameter parameters are designed as shown in Table 2.

Based on a comparison of the numerical calculation results of the above hydraulic diameter parameter design, the best combined outcomes for the flow pulsation, pressure pulsation, and cavitation are considered to be in the range of 85 mm-90 mm with an inlet/outlet ratio of 1. Based on these findings, 87.5 mm has been selected for further investigation in this paper and five groups of hydraulic diameter ratios with different ratios have been designed. The specific designs are shown in Table 3:

Table 3 Parameter configurations for different proportions of hydraulic diameters

Cases	Inlet diameter (mm)	Outlet diameter (mm)	Diameter ratio
1	87.5	52.5	0.6
2	87.5	61.3	0.7
3	87.5	70	0.8
4	87.5	78.8	0.9
5	87.5	87.5	1

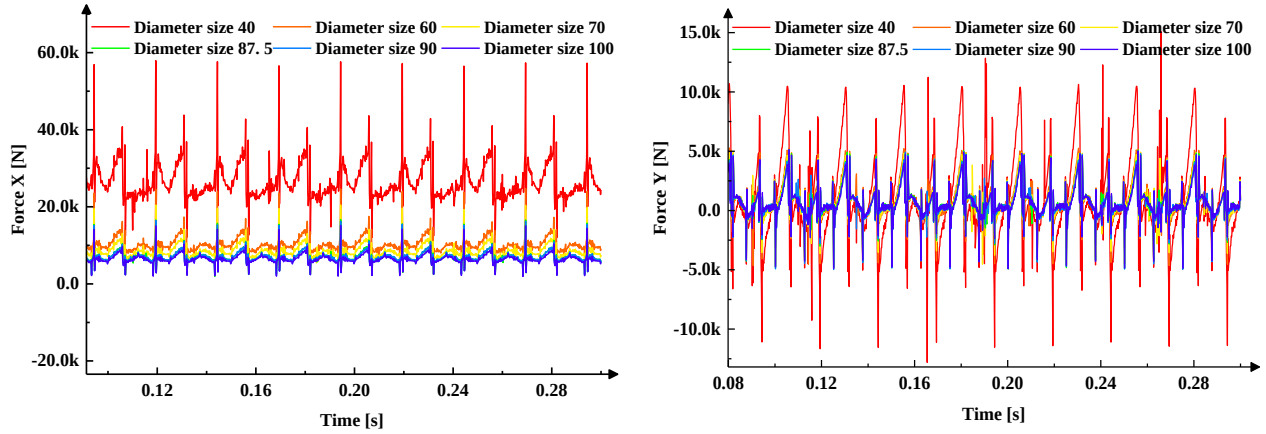

(a) X-direction radial force

(b) Y-direction radial force

Fig. 7 Radial force component and pulsation at a diameter ratio of 1.0

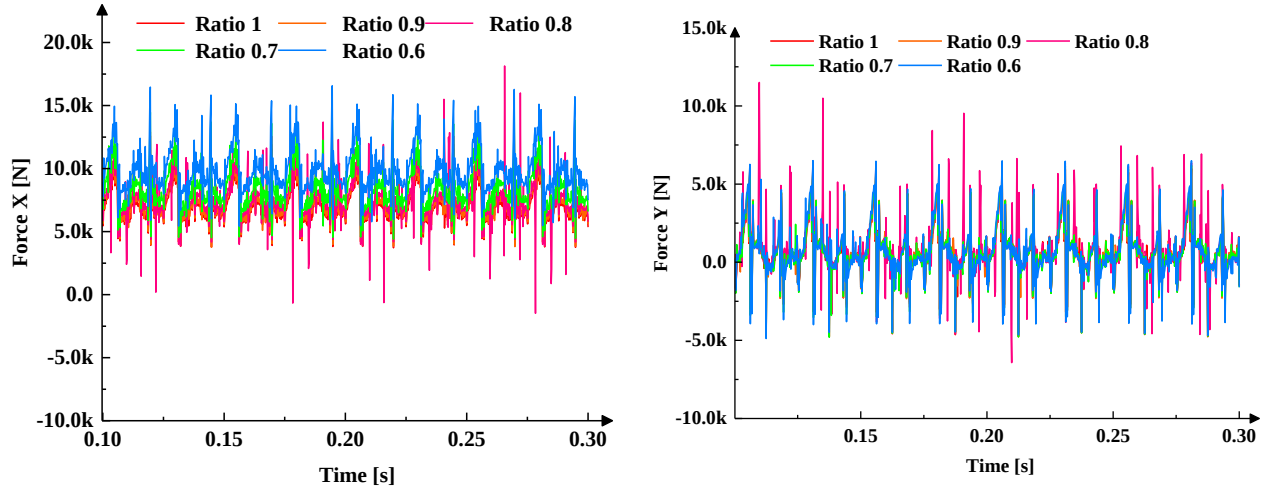

(a) X-direction radial force

(b) Y-direction radial force

Fig. 8 Radial force component and pulsation across varying diameter ratios

4. NUMERICAL SIMULATION RESULTS AND ANALYSIS

4.1 The Influence of Inlet and Outlet Diameters on Shaft Power

Of the factors influencing rotor power, rotor torque and speed play a decisive role. Given that the rotor speed is a constant value, the rotor torque emerges as a significant aspect affecting the rotor power. In this study, only the driving rotor is investigated. Figures 7 and 8 illustrate the forces acting on the rotor in the x and y directions during the rotation of the lobe pump's driving rotor. The geometrical model indicates a zero-pressure component in the z direction (Kang et al., 2012; Amer et al., 2022).

The radial force (F) acting on the rotor is a vector quantity, possessing both magnitude and direction. Eq. 8 illustrates the relationship between the resultant force and its components (Zhao et al., 2023; Chen et al., 2024a). Rotor torque is calculated as force (F) multiplied by the radius of action (R). It follows that the rotor wall pressure affects torque. The higher the combined force of the rotor wall pressures, the greater the rotor torque and the corresponding rotor power. As depicted in Fig. 7, with an increase in the inlet and outlet hydraulic diameters, both the radial force component and its pulsation in the x direction experience an increment. Figure 7 (b) shows that the radial force component in the y direction increases with the expansion of the inlet and outlet diameters, and the radial force component in the y direction pulsation also rises. However, the incremental enlargement in the pressure component is not significant, but rather small when the diameter is expanded to approximately 80 mm. Comparing (a) and (b) in Fig. 9 below confirms that after the inlet diameter is determined, the effect of the outlet diameter on the radial force is relatively small; the average value of is approximately 8000 N, while varies periodically on both sides of the axis. For varying inlet and outlet diameters of the same ratio, the impact on the radial force oscillates within the range of 5000 N-60000 N and fluctuates periodically on both sides of the axis, but the degree of fluctuation is larger compared to different proportions, and the peak value is higher.

$$\begin{cases} \vec{F} = \overrightarrow{F_x} + \overrightarrow{F_y} \\ \left|\vec{F}\right| = \sqrt{\left|\overrightarrow{F_x}\right|^2 + \left|\overrightarrow{F_y}\right|^2} \end{cases} \tag{8}$$

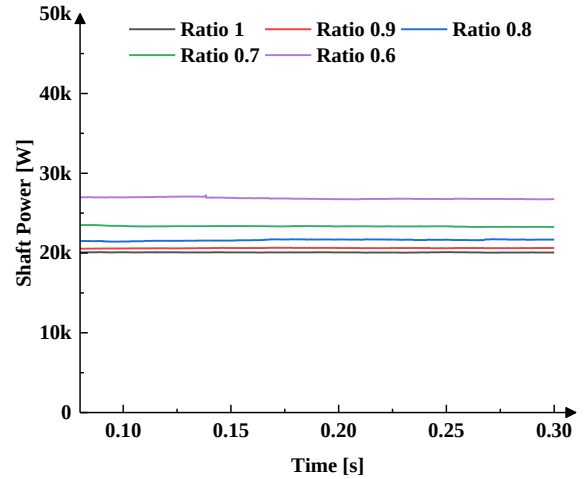

(a) Schematic diagrams of different ratios of shaft power

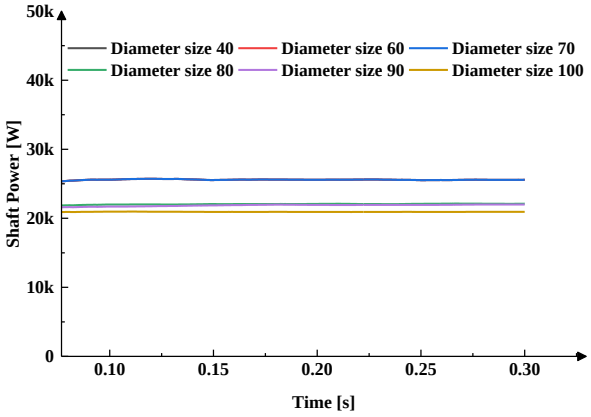

(b) Ratio to 1 shaft power schematic

Fig. 9 Variation of the shaft power with time

Figure 9 presents a linear plot depicting the magnitude of the lobe pump's shaft power during its rotation. Figure 9 (a) compares diameters of the same proportion, while Fig. 9 (b) contrasts five distinct proportions. As illustrated in Fig. 9 (a), the shaft power decreases as the ratio of the inlet to outlet increases. The inlet and outlet flow settings and the size of their inlet and outlet diameters have a significant effect on the shaft power. If the flow is too small and the diameter too large for the pump's power, a test lacking sufficient power will not achieve the set flow rate, and the converse is also true. When the diameters are between 85 mm and 90 mm, the pump achieves stable shaft power. Therefore, it is optimal to set the inlet and outlet diameters within this range. Through the same proportion of different diameter CFD calculations, we take an 85 mm-90 mm middle value of 87.5 mm for the best value of different proportions of the design. Figure 9 (b) shows that the required shaft power drops as the proportion of diameter expands. Outlet diameters of 70 mm, 78.8 mm, and 87.5 mm make the demand for shaft power changes less suitable for practical design.

4.2 The Effect of Inlet and Outlet Diameters on Cavitation in Lobe Pumps

This paper investigated the effect of different inlet and outlet diameters on the cavitation volume distribution inside the lobe pump. Through numerical calculations and

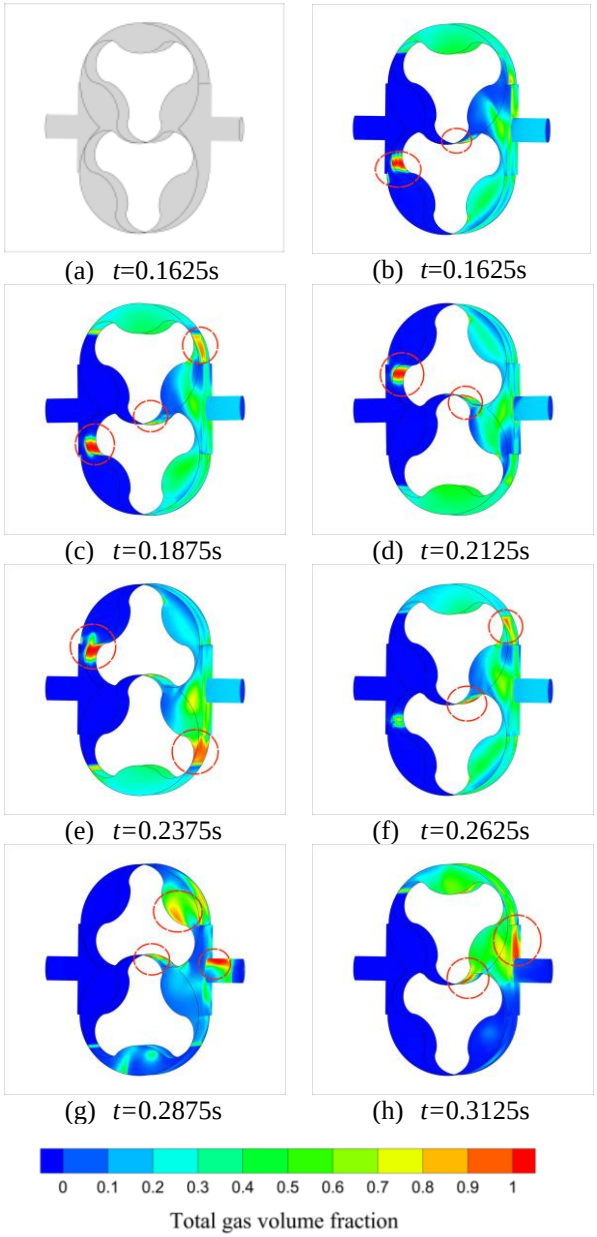

Fig. 10 Variation of total gas volume fraction over a cycle

the post-processing of the previously mentioned experiments, we obtained cloud diagrams depicting the gas volume distribution for different inlet and outlet diameters, as well as flow line diagrams at the gaps. The results are then compared and analysed.

The aforementioned figures present computations conducted in an unsteady state to monitor the changes in cavitation over a week-long rotation of the rotor pump. Figure 10 (a) represents the geometric model, Fig. 10 (b) corresponds to the beginning of the week, and Fig. 10 (h) signifies the end position. Figure 10 (b) depicts the inlet media entering into the pump chamber and the internal rotation of the media forming a collision so that the internal pressure can reduce the formation of the cavitation phenomenon. In Fig. 10 (c) the lobe teeth are driving the media, which are still in a relatively closed pump chamber so that the media pressure is less than the air separation pressure that occurs in the cavitation. However, a small

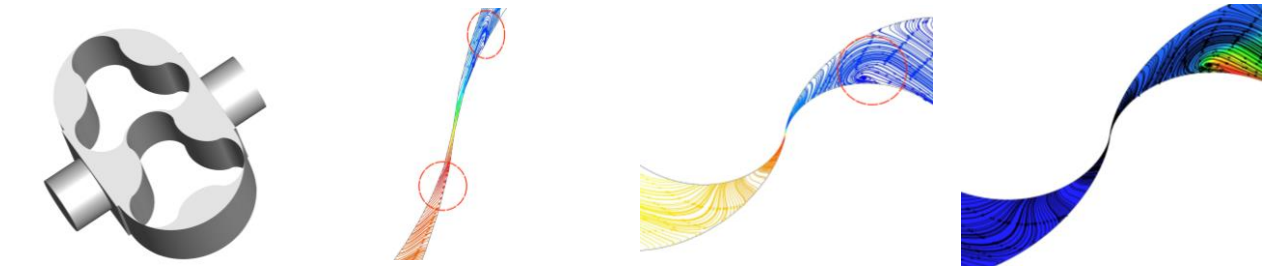

(a) (b) (c) (d)

Fig. 11 Flow line diagram at rotor gap

portion of the cavitation is also due to the pressure of the external vapor pressure being lower than the saturated vapor pressure, so that some of the media vaporize. As illustrated in Fig. 10, most of the cavitation is located in the gap, as are the inlet position and the relative closed position of the pump chamber. Figure 11 below shows an enlarged view of the gap location.

In Fig. 11, the flow line diagram and vector diagrams in the lobe pump rotation gap show a leakage phenomenon, along with the pressure and speed of the rapid change, with the result that the medium and the inlet media collide, thus leading to the vortex phenomenon in Fig. 11 (b) and Fig. 11 (c). The vortex usually produces a negative pressure inside, preventing the normal flow of media. The pressure is lower than the air separation pressure, resulting in cavitation.

The gas volume fraction in the gap is represented in the form of a cloud diagram, as shown in Fig. 12 (a) and (b). Based on the gap plots of 2R = 40, 2R = 60, and 2R = 70 in Fig. 12 (b), the cavitation volume fraction decreases with the increase of the inlet and outlet diameters. The reason for the large cavitation volume fraction is that the overflow area declines drastically, which accelerates the flow rate of the medium, generating a sharp decrease in the external pressure to which the medium is subjected, which is lower than the air separation pressure, and thus gas cavitation occurs. Figure 12 illustrates that during the change in inlet and outlet diameters from large to small, the cavitation volume fraction increases all the way from 0 to 0.8, while the cavitation volume fraction at the tiny gap exhibits a drop from 0.7 to 0.2, and then this rises to 0.8. describes the gap where the leakage develops, culminating in the medium backing up and the formation of convection in the normal flow. This can incite a sharp drop in the flow rate, resulting in a lower than air separation pressure causing cavitation. This may also be due to the high speed of the pump and insufficient oil at the inlet, leading to the lobe pump drawing in inadequate air while forming a gas-liquid dichotomy. From the above analysis, it can be concluded that the sizes of the diameters of the inlet and outlet are set differently when other conditions are at a fixed value. In the case of a sufficient gas volume fraction flow rate, the inlet and outlet diameters are expanded and reduced. When there is insufficient flow, the gas volume fraction grows with an expansion in the inlet and outlet diameters.

4.3 The Impact of the Import and Export Diameters on Pressure Pulsation in Lobe Pumps

Figures 13 and 14 show the pressure variations and their cross-sectional locations. The inlet, outlet, and critical locations are labelled. As depicted in Fig. 13, the pressure at the outlet locations of 85 mm, 90 mm, and 100 mm diameter is relatively balanced, i.e., there is a small pressure difference at the outlet. The pressure difference at 2R = 40 in Fig. 13 appears to be small, but in reality, due to the limited range of the cloud diagram, the actual pressure difference is larger. At the same pressure range, the total pressure at the outlet position can differ by approximately 0.1 MP, which plays a big role in the overall stable operation of the pump. There will be obvious convection on the rotor surface at the outlet, forming a vortex phenomenon.

Figure 14 demonstrates that the outlet pressure balance changes when the ratio deviates from 1. This pressure phenomenon highlights that if the diameter is too small, this leads to a significant increase in pressure and consequently to a reduction in the amount of water withdrawn. If the inlet is too large, although it can increase the amount of water withdrawn, it will waste energy and cause the pump outlet to be oversized, affecting the amount of water that can be withdrawn. If the outlet is too small, although the water will flow faster over a certain distance and the flow rate will increase, the sliding distance will be shortened due to excessive density, culminating in a reduced flow rate. If it is too large, a similar situation to the inlet will occur, resulting in a waste of energy and pumps. Obviously, the design of outlet and inlet diameters cannot simply follow the flow rate. The reasons for this are as follows. (1) If there are stringent requirements for flow rate, speed, and differential pressure and the pump is designed for these ratings, setting the inlet and outlet diameters at the same level will generate an excessive inlet flow rate, while the outlet flow rate may be insufficient. (2) The power of the motor as well as the shaft power of the pump will have an effect on the specific situation, as depicted in Fig. 9. (3) For the pump itself, which has an important influence on cavitation, an inlet and outlet design that is either too large or too small will create larger cavitation bubbles and damage to the pump rotor. There will also be leakage at the gap between the two rotors, which will initiate a convection phenomenon.

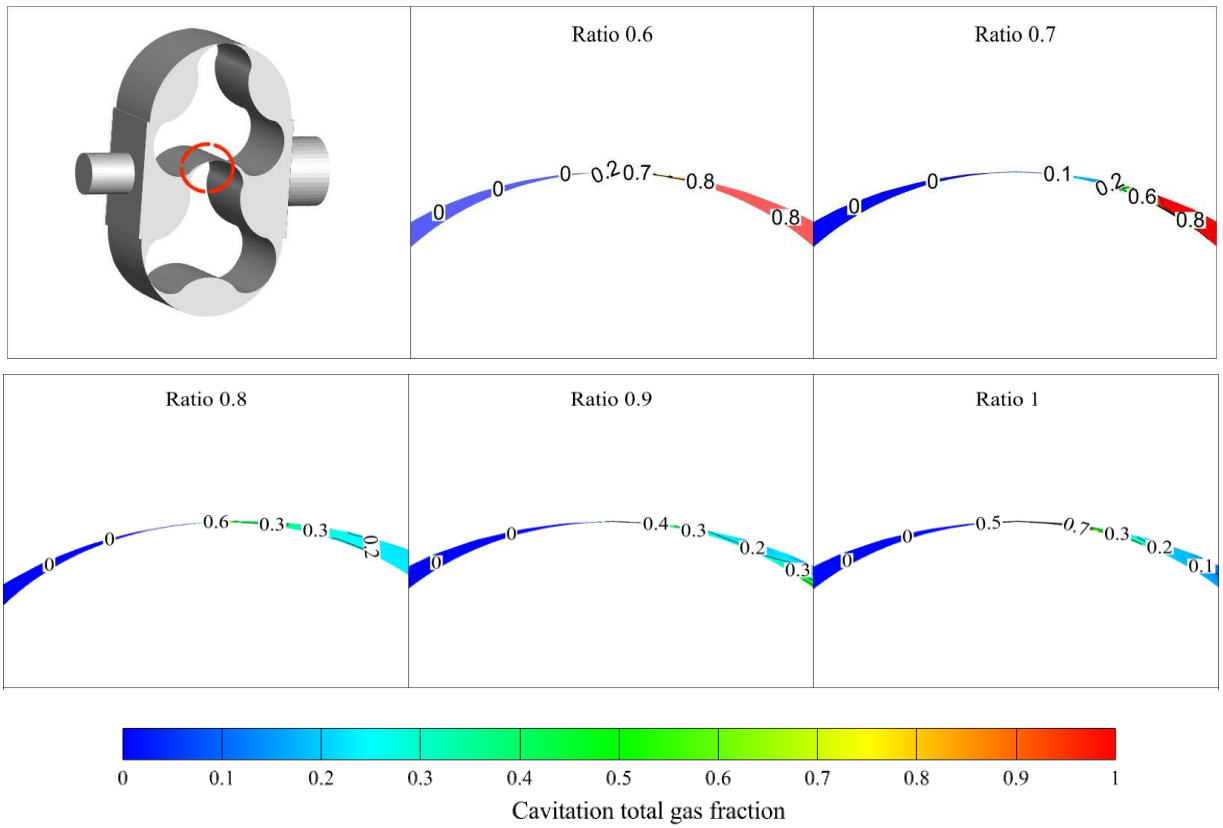

(a) Volume fraction of gas at the gap at the same moment in different ratios

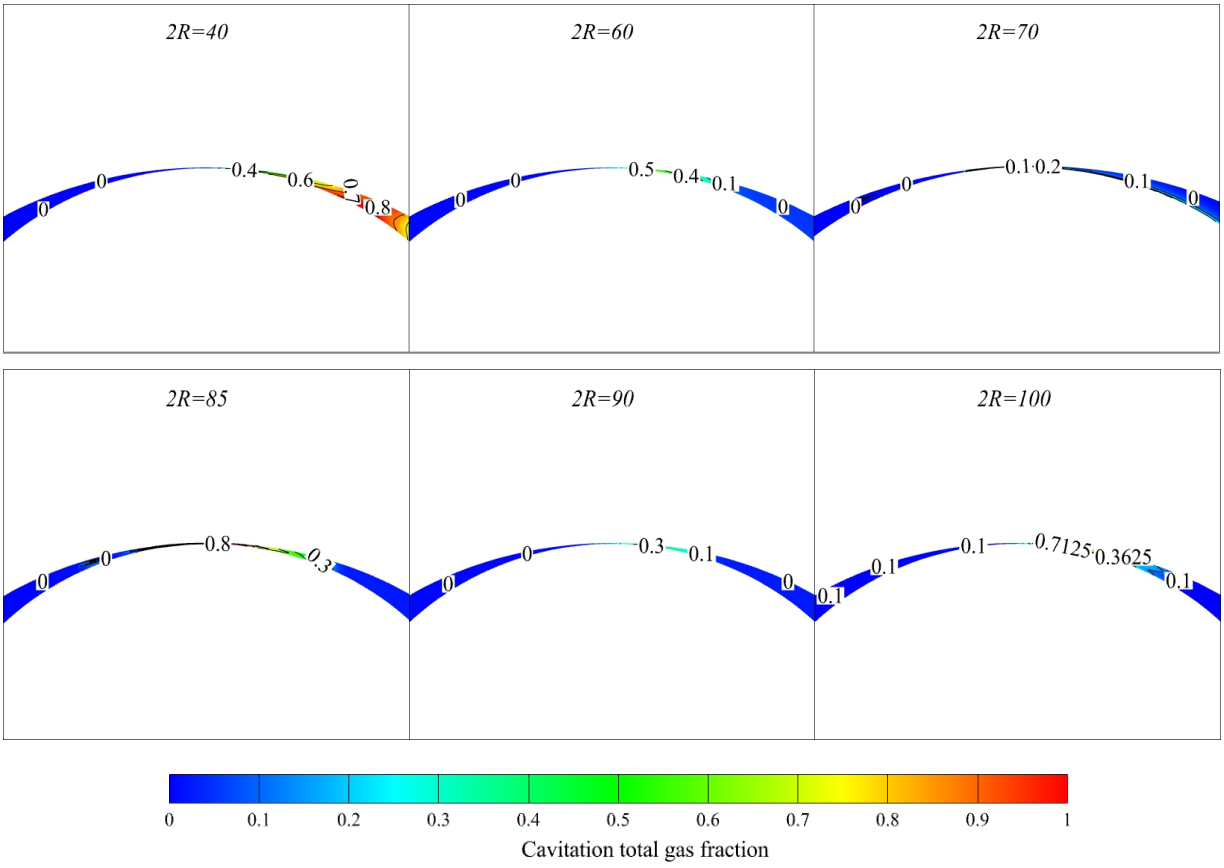

(b) Volume fraction of gas at the gap with ratio 1 at the same time

Fig. 12 Variation of the total gas volume fraction at the gap between rotors

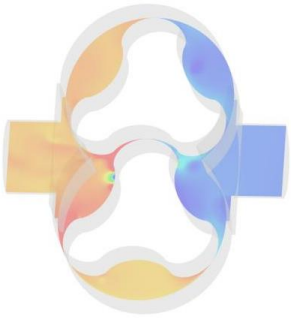

Schematic diagram of x y section location

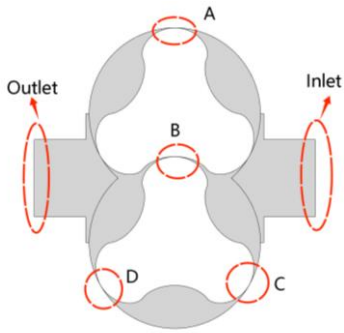

Import and export location schematic

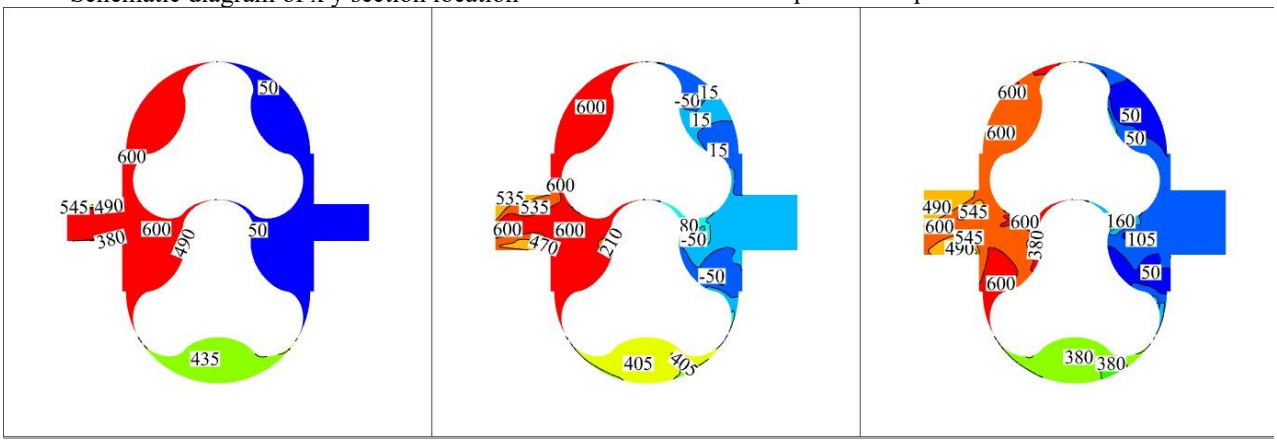

2*R*=40 Pressure contour map | 2*R*=60 Pressure contour map | 2*R*=70 Pressure contour map

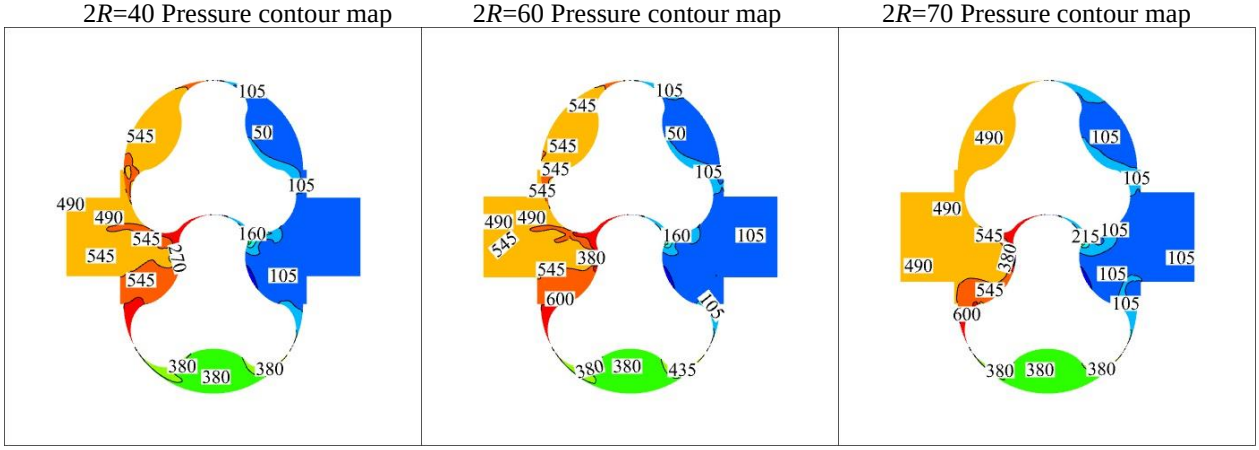

2*R*=85 Pressure contour map | 2*R*=90 Pressure contour map | 2*R*=100 Pressure contour map

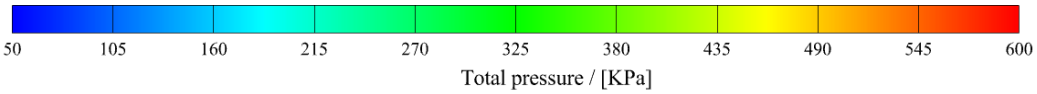

Fig. 13 Pressure distribution when hydraulic diameter size is different in the same proportion

Figure 15 (a) shows the pressure pulsation for an inlet and outlet diameter ratio of 1, but with different inlet and outlet sizes. As the diameter increases, pressure pulsation drops. Figure 15 (a) demonstrates that the pressure pulsation is at its maximum for inlet and outlet diameters of 40 mm. As the import and export diameters decrease, turbulence intensifies, and the reflux phenomenon becomes more pronounced, leading to a rise in pressure pulsation. The situation depicted in Fig. 15 (b) can be obtained from the different ratios of the pressure pulsation of the diameter; with an increase in the ratio, the pressure pulsation falls. In the proportion of 1 the pressure pulsation is at its minimum, and in the proportion of 0.6 it is at its maximum. The ratio of 0.8 to 1 provides the best state.

The intensity of the pressure pulsation is generally expressed in terms of the pressure pulsation coefficient. The pressure pulsation coefficient corresponding to eq. 9 is calculated, and the formula is verified for the above Fig. 15, as well as the large and small pulsations that can be clearly seen (Li et al., 2023, Li et al. 2024c).

$$\delta_F = \frac{F_{\max} - F_{\min}}{F_{\text{ave}}} \tag{9}$$

F_{max} is the maximum instantaneous pressure after stabilization, F_{min} is the minimum instantaneous pressure

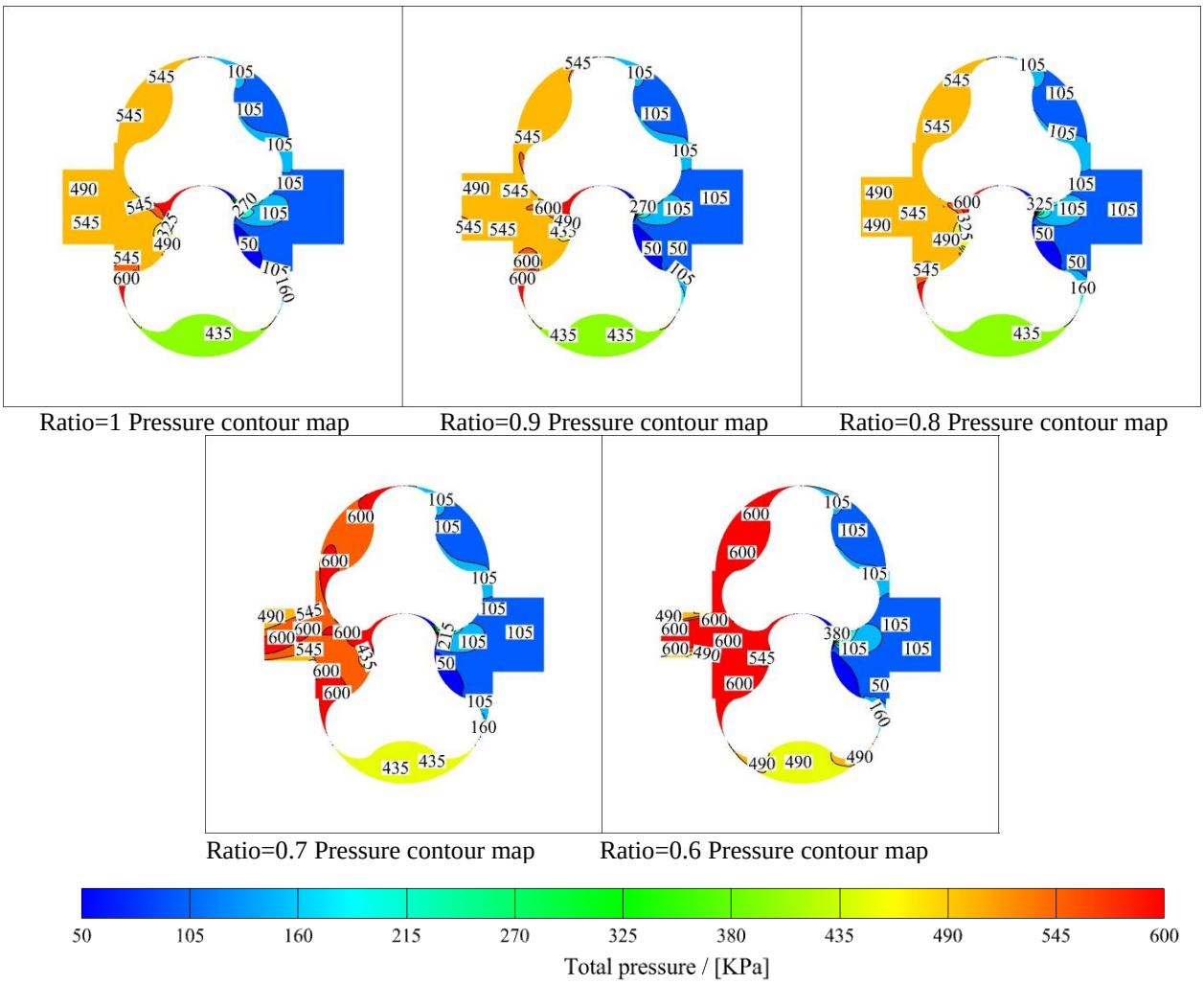

Fig. 14 Pressure distribution change due to different hydraulic diameter ratios

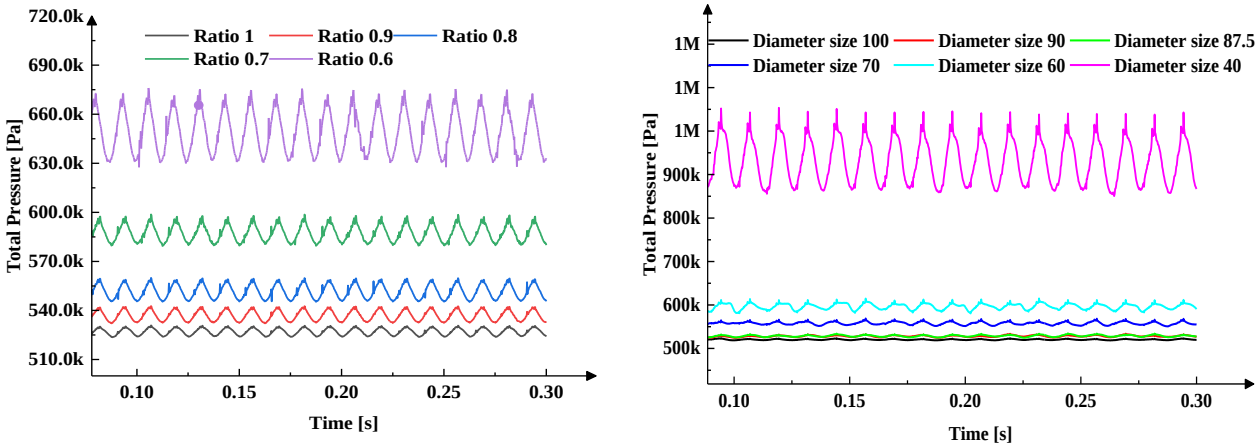

(a) (b)

Fig. 15 Total pressure pulsation over time for varying diameters and ratios

after stabilization, and F_{ave} is the average flow rate after stabilization.

Figure 16 (a) shows the variation of the pressure pulsation coefficient for different ratios and (b) for varying sizes at a ratio of 1. An analysis of Fig. 16 confirms that the ratio of inlet and outlet diameters to the pressure pulsation characteristics of the impeller pump outlet has a significant effect on the latter for different ratios. In the ratio spanning 0.6 to 1, the pressure pulsation coefficient varies from 7.42% to 1.5%, and the pressure pulsation coefficient in the ratio of the smaller pressure pulsation coefficient is larger; in a ratio greater than or equal to 0.7, the pulsation coefficient is bigger. This indicates that the

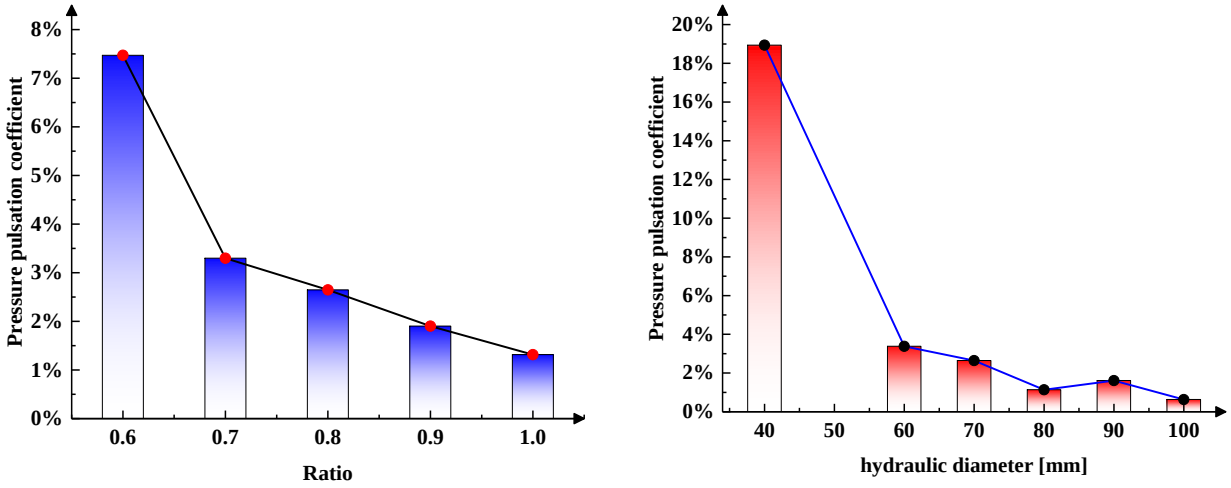

(a) Pressure pulsation coefficient for ratio change of inlet and outlet diameters

(b) Inlet and outlet diameters of different sizes in ratio of 1 pressure pulsation coefficient

Fig. 16 Variation of the pressure pulsation coefficient at the outlet with different diameters

medium flow inside the lobe pump is more stable and has less influence on the flow inside the lobe pump. The pressure pulsation coefficient tends to decrease at the same ratio for diameters ranging from 40 mm to 100 mm. After a diameter of more than 60 mm, the pulsation coefficient drops more slowly and stabilizes at approximately 1%-2%, indicating that this design is acceptable. In the design process, we cannot rely solely on the flow rate for the sake of simplicity and convenience when designing the pump diameter.

5. CONCLUSIONS

The influence of the lobe pump's inlet and outlet diameters on shaft power, cavitation, and pressure pulsation was analysed through simulations with six groups of equal proportions but varying sizes, as well as five groups with different proportions. The conclusions are summarized as follows.

1）A comparison of the shaft power graphs for pumps with different inlet and outlet diameter ratios and pumps with the same diameter but different sizes shows that for pumps with the same inlet and outlet diameters, the shaft power tends to decrease from 25.5 kW to 21 kW for diameters increasing from 40 to 100 mm. Moreover, the shaft power tends to stabilize when the diameter is between 70 mm and 90 mm. On the contrary, as the ratio of inlet and outlet diameters increases, the shaft power gradually increases and stabilizes at a ratio of 0.7-0.9. Increasing the inlet and outlet diameters changes the rotor radial force and reduces the resistance of the fluid in the pipework, thus reducing the power demand of the pump. Considering the unilateral factor of shaft power, the above conclusion shows that when the ratio of inlet and outlet diameters is 1, the size of inlet and outlet diameters is set to be 0.7 to 0.9 times the thickness of the rotor is the best, and when the ratio of inlet and outlet diameters is not 1, the ratio of inlet and outlet diameters is set to be 0.7 to 0.9 is the best.

2）By comparing the pressure pulsation diagrams and pulsation coefficient diagrams of pumps with different inlet-to-outlet diameter ratios, as well as pumps with equal inlet and outlet diameters but differing sizes, it is observed that when the inlet and outlet diameter ratio is 1, the pulsation coefficient shows a significant decrease as the diameter increases from 40 mm to 100 mm, dropping from 18.5% to approximately 1%. The shaft power also stabilizes for diameters between 70 mm and 100 mm. For varying diameter ratios, the pressure pulsation coefficient decreases with increasing ratios and reaches a steady state at a ratio of 0.7-0.9. Enlarging the inlet and outlet diameters reduces fluid resistance within the pump, minimizing flow rate and pressure fluctuations, thereby reducing the risk of cavitation. Conversely, smaller inlet diameters lead to higher fluid velocity and pressure fluctuations, raising the likelihood of cavitation.

3) As the ratio of the inlet and outlet diameters increases, a clear increase in rotor pulsation amplitude in the x and y directions is observed. When the ratio reaches 1, the maximum value of radial force in X direction decreases from 17.63 kN to 12.52 kN, and the maximum value of radial force in Y direction decreases from 7.68 kN to 6.32 kN. When the ratio reaches 1, the peak pulsation amplitude is at its maximum, while the variation trend decreases when the ratio is between 0.7 and 0.9. Additionally, as the inlet and outlet diameters expand from 40 mm to 100 mm, the maximum value of radial force in the X direction decreased from 58.36 kN to 17.6 kN, and the maximum value of radial force in the Y direction decreased from 14.56 kN to 3.25 kN. The amplitude of pulsation in the x and y directions gradually drops and stabilizes at diameters between 70 mm and 100 mm.

Based on the above study, if the same inlet and outlet dimensions are required, the inlet and outlet of the pump can be adjusted by forward and reverse rotation of the motor, and the inlet and outlet diameters should be set to 0.7 to 0.9 times the rotor thickness. If the position of the inlet and outlet is not adjusted, the inlet diameter should be larger than the outlet, and the outlet diameter should be

0.7 to 0.9 times the inlet diameter. The correctness of the numerical simulation can then be confirmed through experiments, facilitating more in-depth studies. At present, research focuses not only on the size of the inlet and outlet but also on coupling the inlet and outlet positions with the rotor area, examining structural features such as rounded corners and right angles, together with their respective sizes.

ACKNOWLEDGEMENTS

The authors gratefully acknowledge the financial support provided by the Open Research Fund of Key Laboratory of River Basin Digital Twinning of Ministry of Water Resources (Grant No. Z0202042022), Fundamental Research Funds for the Provincial Universities of Zhejiang (2023YW98), and Zhejiang Provincial Science and Technology Plan Project of China (Grant No.2022C02035).

CONFLICT OF INTEREST

The authors declare that they have no known competing financial interests or personal relationships

AUTHORS CONTRIBUTION

Hengzhi Zhou： software, Data Curation, Formal analysis, Writing-Original Draft, Visualization. **Peijian Zhou ：** Conceptualization, Methodology, Funding acquisition; Supervision; Resources; Conceptualization – Ideas (supporting). **Long Meng：** Conceptualization, Methodology, Funding acquisition; Supervision; Resources. **Jian Li:** Supervision; Resources; Conceptualization – Ideas (supporting). **Chun Xiang:** Supervision; Resources; Ideas (supporting). **Heng Qian:** Supervision, Writing - Review & Editing.

REFERENCES

Al-Obaidi, A. R. (2024a). Effect of different guide vane configurations on flow field investigation and performances of an axial pump based on CFD analysis and vibration investigation. *Experimental Techniques*, *48*(1), 69–88. https://doi.org/10.1007/s40799-023-00641-5

Al-Obaidi, A. R. (2024b). Evaluation and investigation of hydraulic performance characteristics in an axial pump based on CFD and acoustic analysis. *Processes*, *12*(1), 129. https://doi.org/10.3390/pr12010129

Al-Obaidi, A. R., & Alhamid, J. (2024). Analysis of unsteady internal flow characteristics in axial pump with varying number of blades using computational modelling and vibration techniques. *Flow Measurement and Instrumentation*, *99*, 102654. https://doi.org/10.1016/j.flowmeasinst.2024.102654

Al-Obaidi, A. R., Alhamid, J., & Khalaf, H. (2024). Unsteady behaviour and plane blade angle configurations' effects on pressure fluctuations and internal flow analysis in axial flow pumps. *Alexandria Engineering Journal*, *99*, 83–107. https://doi.org/10.1016/j.aej.2024.04.048

Amer, M., Vaca, A., & Bowden, M. (2022). Effects of different blade numbers on radial exciting force of lobe pump rotor: Original papers. *Bioprocess and Biosystems Engineering*, *45*(9), 1477–1488. https://doi.org/10.1007/s00449-022-02757-1

Ammendolea, D., Greco, F., Leonetti, L., Lonetti, P., & Pascuzzo, A. (2023). Fatigue crack growth simulation using the moving mesh technique. *Fatigue & Fracture of Engineering Materials & Structures*, *46*(12), 4606–4627. https://doi.org/10.1111/ffe.14155

Bonandrini, G., Mimmi, G., & Rottenbacher, C. (2012). Design and simulation of meshing of a particular internal rotary pump. *Mechanism and Machine Theory*, *49*, 104–116. https://doi.org/10.1016/j.mechmachtheory.2011.11.001

Chen, J., Zhang, M., Liu, T., Huang, B., Wang, Y., & Hu, C. (2024a). Experimental investigation of the influence of micro vortex generator on the bubble cavitation around a hydrofoil. *Ocean Engineering*, *298*, 117216. https://doi.org/10.1016/j.oceaneng.2024.117216

Chen, J., Zhang, M., Liu, T., Huang, B., Wang, Y., & Hu, C. (2024b). Experimental investigation of the influence of micro vortex generator on the bubble cavitation around a hydrofoil. *Ocean Engineering*, *298*, 117216. https://doi.org/10.1016/j.oceaneng.2024.117216

Dehghan, A. A., & Shojaeefard, M. H. (2022). Experimental and numerical optimization of a centrifugal pump volute and its effect on head and hydraulic efficiency at the best efficiency point. *Proceedings of the Institution of Mechanical Engineers Part C-Journal of Mechanical Engineering Science*, *236*(9), 4577–4598. https://doi.org/10.1177/09544062211056019

Dehghan, A. A., Shojaeefard, M. H., & Roshanaei, M. (2024). Exploring a new criterion to determine the onset of cavitation in centrifugal pumps from energy-saving standpoint; experimental and numerical investigation. *Energy*, *293*, 130681. https://doi.org/10.1016/j.energy.2024.130681

Gu, P., Xing, L., Wang, Y., Feng, J., & Peng, X. (2021). Transient flow field and performance analysis of a claw pump for FCVs. *International Journal of Hydrogen Energy*, *46*(1), 984–997. https://doi.org/10.1016/j.ijhydene.2020.09.154

Hatano, S., Kang, D., Kagawa, S., Nohmi, M., & Yokota, K. (2014). Study of cavitation instabilities in double-suction centrifugal pump. *International Journal of Fluid Machinery and Systems*, *7*(3), 94–100. https://doi.org/10.5293/IJFMS.2014.7.3.094

Jacazio, G., & De Martin, A. (2016). Influence of rotor profile geometry on the performance of an original

low-pressure gerotor pump. *Mechanism and Machine Theory*, *100*, 296–312. https://doi.org/10.1016/j.mechmachtheory.2016.02.012

Kang, Y. H., Vu, H. H., & Hsu, C. H. (2012). Factors impacting on performance of lobe pumps: a numerical evaluation. *Journal of Mechanics*, *28*(2), 229–238. https://doi.org/10.1017/jmech.2012.26

Li, G., Sun, H., He, J., Ding, X., Zhu, W., Qin, C., Zhang, X., Zhou, X., Yang, B., & Guo, Y. (2024a). Deep learning, numerical, and experimental methods to reveal hydrodynamics performance and cavitation development in centrifugal pump. *Expert Systems with Applications*, *237*, 121604. https://doi.org/10.1016/j.eswa.2023.121604

Li, J., Wu, T., Cheng, C., Li, J., & Zhou, K. (2024b). A Review of the research progress and application of key components in the hydrogen fuel cell system. *Processes*, *12*(2), 249. https://doi.org/10.3390/pr12020249

Li, Y., Li, W., Ji, L., He, S., Huang, Y., Li, S., Zhai, H., Pu, W., & Li, X. (2024c). Analysis of internal flow characteristics in hydrogen circulation pump with variable trochoid ratio profile. *International Journal of Hydrogen Energy*, *61*, 1429–1445. https://doi.org/10.1016/j.ijhydene.2024.02.288

Li, S., Li, W., Ji, L., Zhai, H., Li, Y., Wang, C., & Li, X. (2023). Effect of pressure ratio on transient flow in hydrogen circulating pump. *International Journal of Hydrogen Energy*, *48*(69), 26937–26950. https://doi.org/10.1016/j.ijhydene.2023.03.370

Li, Y., Guo, D., & Li, X. (2019). The effect of startup modes on a vacuum lobe pump. *Vacuum*, *166*, 170–177. https://doi.org/10.1016/j.vacuum.2019.05.009

Li, Y., Zhang, X., Guo, D., Wang, X., (2018). Numerical analysis and verification of flow characteristics of rotor cavity of spiral rotary lobe pump, Transactions of the Chinese Society of Agricultural Engineering. 2018,34(10):62-67. https://doi.org/10.11975/j.issn.1002-6819.

Liersch, C., Frankenbach, M., Froehlich, J., & Lang, J. (2014). Recent progress in designing moving meshes for complex turbulent flows. *Meteorologische Zeitschrift*, *23*(4), 425–439. https://doi.org/10.1127/0941-2948/2014/0573

Liu, G., Liu, P. Y., Wei, W. J., Zhang, S. Y., & Li, H. T. (2012). A New design method for the rotor profile curve of the lobe pump. *Advanced Materials Research*, *482–484*, 1196–1200. https://doi.org/10.4028/www.scientific.net/AMR.482-484.1196

Liu, Y., Wang, L., & Zhu, Z. (2015). Numerical study on flow characteristics of rotor pumps including cavitation. *Proceedings of the Institution of Mechanical Engineers, Part C: Journal of Mechanical Engineering Science*, *229*(14), 2626–2638. https://doi.org/10.1177/0954406214562634

Luo, H., Zhou, P., Cui, J., Wang, Y., Zheng, H., & Wang, Y. (2025). Energy performance prediction of centrifugal pumps based on adaptive support vector regression. *Engineering Applications of Artificial Intelligence*, *145*, 110247. https://doi.org/10.1016/j.engappai.2025.110247

Malekshah, E. H., Wlodzimierz, W., & Majkut, M. law. (2024). Investigation on natural to ventilated cavitation considering the air-vapor interactions by Merging theory with insight on air jet location/rate effect. *International Journal of Heat and Mass Transfer*, *220*, 124968. https://doi.org/10.1016/j.ijheatmasstransfer.2023.124968

Matteo, L., Dazin, A., & Tauveron, N. (2019). Modelling of a centrifugal pump using the CATHARE-3 one-dimensional transient rotodynamic pump model. *International Journal of Fluid Machinery and Systems*, *12*(2), 147–158. https://doi.org/10.5293/IJFMS.2019.12.2.147

Menendez Blanco, A., & Fernandez Oro, J. M. (2012). Unsteady numerical simulation of an air-operated piston pump for lubricating greases using dynamic meshes. *Computers & Fluids*, *57*, 138–150. https://doi.org/10.1016/j.compfluid.2011.12.014

Meng, X., Tian, H., Yu, R., Lu, Y., Gu, X., Tan, G., & Cai, G. (2023). Three-dimensional numerical simulation of hybrid rocket motor based on dynamic mesh technology. *Aerospace Science and Technology*, *141*, 108573. https://doi.org/10.1016/j.ast.2023.108573

Orlandi, F., Muzzioli, G., Milani, M., Paltrinieri, F., & Montorsi, L. (2023). Development of a numerical approach for the CFD simulation of a gear pump under actual operating conditions. *Fluids*, *8*(9), 244. https://doi.org/10.3390/fluids8090244

Qiu, J. T., Li, N., Yang, C. J., Cai, Y. L., & Meng, K. Y. (2022). Numerical study on a coupled viscous and potential flow design method of axial-flow pump impeller. *Ocean Engineering*, *266*, 112720. https://doi.org/10.1016/j.oceaneng.2022.112720

Sun, S., Wang, X., Guo, P., Wu, K., Luo, X., & Liu, G. (2022). Numerical analysis of the transient leakage flow in axial clearance of a scroll refrigeration compressor. *Proceedings of the Institution of Mechanical Engineers, Part E: Journal of Process Mechanical Engineering*, *236*(1), 47–61. https://doi.org/10.1177/0954408919870910

Vande Voorde, J., Vierendeels, J., & Dick, E. (2004). Flow simulations in rotary volumetric pumps and compressors with the fictitious domain method. *Journal of Computational and Applied Mathematics*, *168*(1–2), 491–499. https://doi.org/10.1016/j.lobe.2003.04.007

Wang, J., Liu, R., Yang, S., Li, H., Wang, Z., & Li, Q. (2018). Geometric study and simulation of an elliptical rotor profile for Roots vacuum pumps.

Vacuum, *153*, 168–175. https://doi.org/10.1016/j.vacuum.2018.04.014

Xu, B., Liu, Q., Zhu, Z., Gao, Y., Li, C., & Zhang, Y. (2024). Influence of the rotation speed on the internal flow characteristics of an aircraft fuel gear pump. *Processes*, *12*(3), 576. https://doi.org/10.3390/pr12030576

Zhai, H., Li, W., Ji, L., Awais, M., Li, J., & Li, S. (2022). Profile design and performance research of hydrogen circulation pump in fuel cell system. *Mechanics*, *28*(4), 283–293. https://doi.org/10.5755/j02.mech.31528

Zhang, Q., Feng, J., Zhang, Q., & Peng, X. (2019). Performance prediction and evaluation of the scroll-type hydrogen pump for FCVs based on CFD–Taguchi method. *International Journal of Hydrogen Energy*, *44*(29), 15333–15343. https://doi.org/10.1016/j.ijhydene.2019.04.019

Zhao, Y., Li, G., Zhao, F., Wang, X., & Xu, W. (2023). Analysis of macroscopic cavitation characteristics of a self-excited oscillating cavitation jet nozzle. *Journal of Applied Fluid Mechanics*, *16*(11), 2130–2141. https://doi.org/10.47176/jafm.16.11.1923

Zhou, P., Cui, J., Xiao, G., Xiang, C., Dai, J., & Zheng, S. (2023). Numerical study on cavitating flow-induced pressure fluctuations in a gerotor pump. *Energies*, *16*(21), 7301. https://doi.org/10.3390/en16217301

Zhou, P., Wen, Z., Wang, Y., Wu, Y., Wu, D., Huang, R., & Yao, Z. (2025). Improving the energy performance of vortex pump based on whale optimization algorithm. *Engineering Applications of Computational Fluid Mechanics*, *19*(1), 2441344. http://doi.org/10.1080/19942060.2024.2441344